

Research Article

Estimation of the Squirt-Flow Length Based on Crack Properties in Tight Sandstones

Chunfang Wu,¹ Jing Ba ,¹ Lin Zhang,¹ and José M. Carcione^{1,2}

¹School of Earth Sciences and Engineering, Hohai University, Nanjing 211100, China

²Istituto Nazionale di Oceanografia e di Geofisica Sperimentale (OGS), Borgo Grotta Gigante 42c, 34010 Sgonico, Trieste, Italy

Correspondence should be addressed to Jing Ba; jba@hhu.edu.cn

Received 11 June 2021; Accepted 30 November 2021; Published 12 January 2022

Academic Editor: Feng Cheng

Copyright © 2022 Chunfang Wu et al. Exclusive Licensee GeoScienceWorld. Distributed under a Creative Commons Attribution License (CC BY 4.0).

Tight sandstones have low porosity and permeability and strong heterogeneities with microcracks, resulting in small wave impedance contrasts with the surrounding rock and weak fluid-induced seismic effects, which make the seismic characterization for fluid detection and identification difficult. For this purpose, we propose a reformulated modified frame squirt-flow (MFS) model to describe wave attenuation and velocity dispersion. The squirt-flow length (R) is an important parameter of the model, and, at present, no direct method has been reported to determine it. We obtain the crack properties and R based on the DZ (David-Zimmerman) model and MFS model, and how these properties affect the wave propagation, considering ultrasonic experimental data of the Sichuan Basin. The new model can be useful in practical applications related to exploration areas.

1. Introduction

Tight (oil and gas) reservoirs are becoming important in seismic exploration [1–3], with tight sandstones playing a dominant role in China, since they are widely distributed. Unlike conventional reservoirs, tight sandstone ones have a complex geological origin, low porosity and permeability, and strong heterogeneities with a complex pore structure. In recent years, a series of studies have been performed related to the characterization of these rocks [4–8].

The pore structure of the reservoirs affects the oil and gas distribution [9]. Cracks not only affect the elasticity of the rocks, but also the fluid flow [10–13]. Zimmerman [14] presented an empirical relation between the compressibility and effective pressure of sandstones and David and Zimmerman [15] extended the method to predict the crack distribution from dry-rock wave velocities (DZ model) on the basis of the MT [16] and DEM [17] models. Deng et al. [18] investigated the pore structure of conventional and tight sandstones based on the DZ model, and Wei et al. [19] studied the influence of effective pressure and porosity on the crack properties.

Wave propagation in earth crust is often accompanied by significant attenuation and dispersion [20–23], and many theoretical models have been proposed [11, 24–27]. With new developments and analyses on field measured data, it has been realized that local fluid flow induced by heterogeneities is the main cause of dissipation [28]. Based on the Biot theory [29–31], the BISQ model [32] introduced a new property called “squirt-flow length” to describe the squirt flow and combined the effects at macroscopic (Biot’s) and microscopic scales. The fast P-wave velocity dispersion predicted by the model is significantly higher than that of the Biot model. However, the fast P-wave velocity is lower than the Gassmann velocity [33] at low frequencies and is consistent with the high-frequency one predicted by the Biot theory. Mavko and Jizba [34] proposed an equation (M-J model) based on a modified rock skeleton to compute the elastic modulus of the unrelaxed wet-rock skeleton at high frequencies. The P-wave velocity predicted by the M-J model is greater than that of the Biot model at high frequencies and also greater than the Gassmann velocity at low frequencies. This equation is not applicable to the case of gas-saturated or dry rocks. In view of the limitations of the M-J model,

Gurevich et al. [35] extended it based on the theory of Murphy et al. [36], which can be applied at all frequencies. Li et al. [37] pointed out that the characteristic frequency of squirt flow is related to the crack aspect ratio, fluid viscosity, and bulk moduli of the minerals. Carcione and Gurevich [38] unified the squirt-flow and Biot theories and performed numerical simulations based on the Zener mechanical model [39].

Dvorkin et al. [40] obtained the complex modulus of fluid-saturated rocks based on the BISQ mode by considering a one-dimensional radial flow. This theory is consistent with the Gassmann velocity at the low-frequency limit. However, the model does not consider the influence of the Biot flow. In addition, the P-wave velocity obtained with this model is higher than the theoretical maximum value at high frequencies (when all the cracks are closed, and the P-wave velocity value is determined by the Biot model) [41]. To overcome these problems, Wu et al. [41] presented the MFS model.

The parameter R is crucial in the squirt-flow model, but to date, it has not been obtained by direct experiments, and this restricts the use of the theory [42]. Dvorkin et al. [43] showed that this parameter represents the radius of a cylinder with its axis parallel to the direction of wave propagation. Based on ultrasonic experimental data of Best [44], Marketos and Best [45] found that the relation between R and viscosity follows a power law. Since the BISQ model was proposed, other studies have been performed, which mainly focused on extending the model [40, 41, 46–48], considering anisotropy [28, 49] and wave simulation [50–52]. However, the approach about how to determine R remains unclear.

First, we use ultrasonic experimental data of tight sandstones and apply the DZ model to analyze the crack distribution. Then, R is obtained with the MFS model. We analyze the relations between R and crack density, crack aspect ratio, permeability, and other properties. A semiempirical formula of R for tight sandstones is proposed.

2. Ultrasonic Experimental Data and Results

Tutuncu et al. [53] showed that there is a close contact between adjacent grains in tight sandstone, and a large number of cracks are formed at the edges of grains. We select twelve tight sandstone samples, collected from the Upper Triassic Xujiache Formation in the Guang'an gasfield of the central Sichuan Basin. This sandstone is one of the greatest potential strata in this basin, whose reservoirs are characterized by low porosity and permeability, well-developed cracks, and high-water saturation. The samples are mainly lithic quartz sandstone, with a small amount of siliceous quartz sandstone, which is composed of quartz, feldspar, lithic debris, and cements. The porosity ranges from 3% to 14%, and the bulk modulus of the mineral is 39 GPa. The rock samples were processed into cylinders with a diameter of 25 mm and a height of 25 to 50 mm, and both ends of the sample were polished. The experimental set-up consists of a pulse generator, a temperature control unit, a confining pressure control unit, a

TABLE 1: Properties of the tight sandstones in Guang'an area.

Sample	Porosity (%)	Permeability (mD)	Grain density (kg/m ³)
GAR11	3.03	0.001	2687
GA3	3.46	0.005	2694
GAR1	4.19	0.0005	2676
GA10	4.89	0.004	2691
GA6	6.26	0.046	2672
GAR6	6.33	0.047	2665
GA8	8.55	0.082	2670
GAR7	8.65	0.028	2668
GAR12	8.97	0.14	2662
GA1	13.26	1.21	2659
GAR8	13.35	1.320	2653
GA2	13.91	1.370	2660

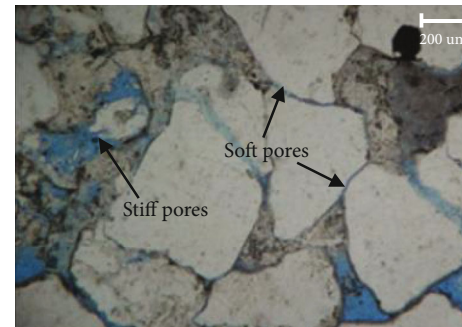


FIGURE 1: Thin-section image of the tight sandstone.

pore pressure control unit, and an acoustic wave test unit [54, 55].

For the tests with full gas saturation (nitrogen), the samples were sealed with a rubber sleeve. The pore pressure was 10 MPa, and effective pressures of 5, 10, 15, 20, 25, 30, and 35 MPa were applied. The transmitted waveforms were recorded at 80°C, by maintaining the experimental conditions for half an hour. Then, the samples were saturated with brine (146,377 ppm NaCl) by vacuum pumping pressurization. The velocities at different effective pressures were obtained from the first arrivals of the extracted waveforms. The errors of the velocity measurement are estimated according to Yurikov et al. [56], and they are in range of 0.242–0.465%. The rock properties are given in Table 1.

A thin-section analysis of the sample is shown in Figure 1, where blue-dyed resin indicates porosity and microcracks/contacts are observed.

Figures 2 and 3 show the S- and P-wave velocities, respectively, as a function of the effective pressure at full gas and water saturations. The P- and S-wave velocities are higher in the second case, increasing with pressure. Some water-saturated tight samples show a greater S velocity than the gas-saturated state, which is related to the heterogeneous

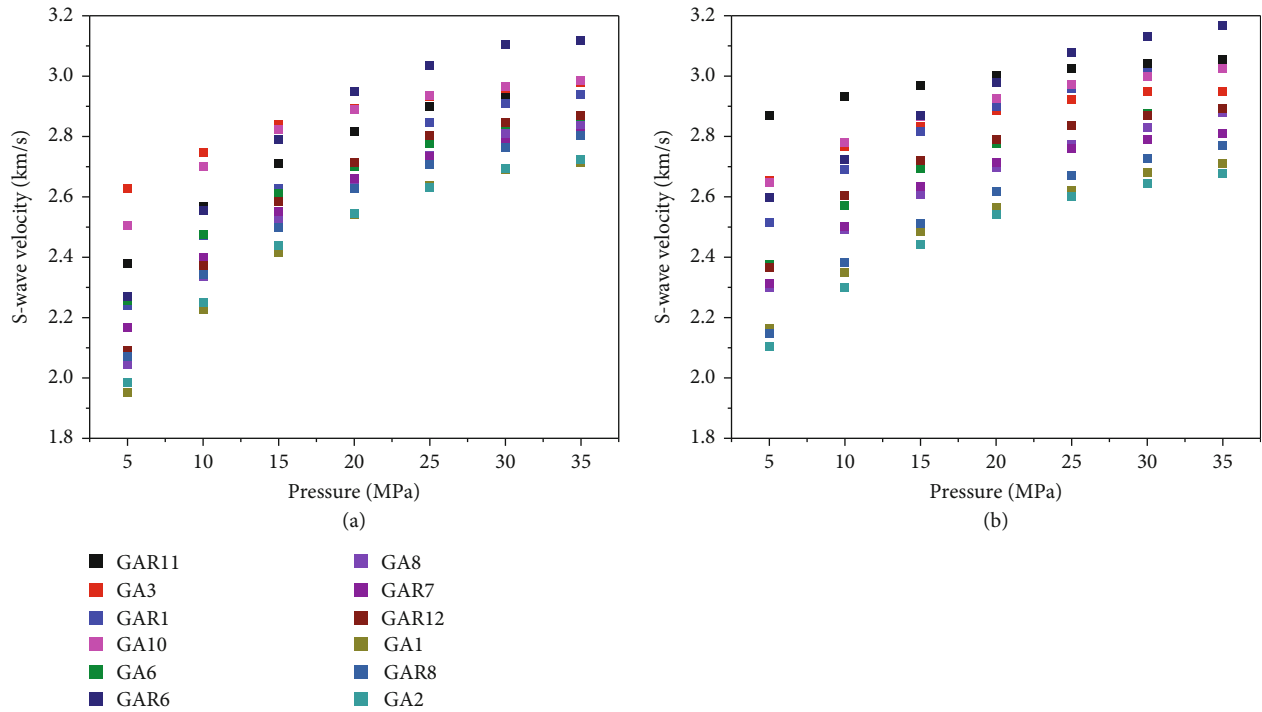


FIGURE 2: (a, b) S-wave velocity as a function of the effective pressure at full gas and water saturations.

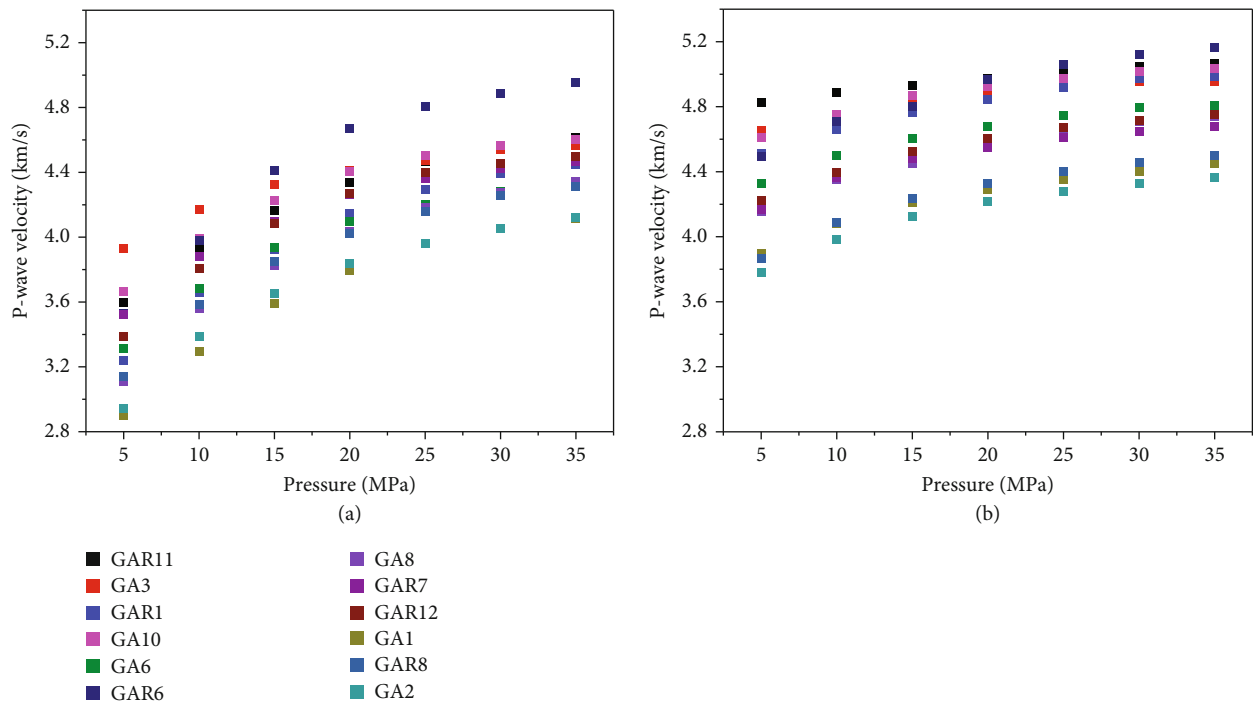


FIGURE 3: (a, b) P-wave velocity as a function of the effective pressure at full gas and water saturations.

microcracks and microstructures. For tight rocks, the stiffening effect of local fluid flow on rock skeleton, which is induced by S-waves at high frequencies, may also lead to a

higher S-wave velocity at the water-saturated state [55]. In the low-pressure range, the rate of velocity variation with pressure is significant and then decreases with increasing

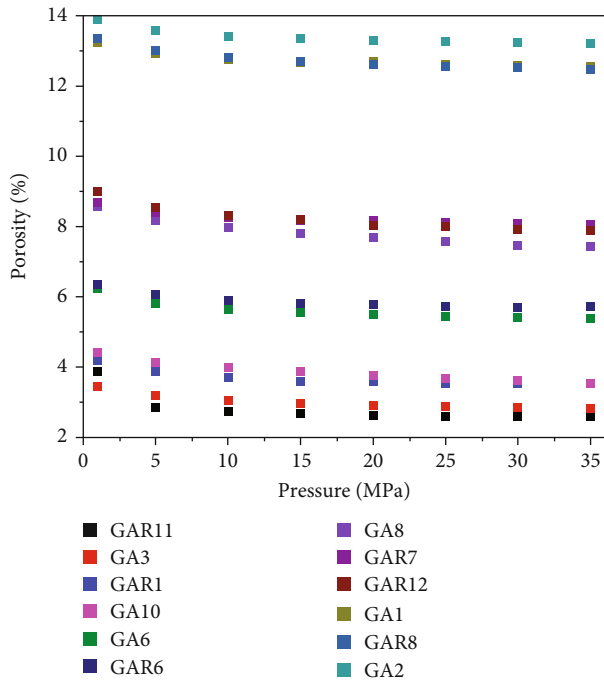


FIGURE 4: Porosity as a function of the effective pressure.

pressure (e.g., [18, 57], and [58]). The main reason is that the cracks close when effective pressure increases. The influence of pressure on the stiff pores is small and can be neglected [15, 59], so that the velocities as a function of the pressure can be used to obtain the crack properties.

The different pressures cause the porosity changes, and the change of crack porosity is dominant. The porosities of the sandstones as a function of the effective pressure are shown in Figure 4, where we can see that porosity decreases with increasing pressure. The porosity variation is more significant in the low-pressure range, which is caused by the closure of cracks when pressure increases. At high pressures, the porosity variation diminishes.

3. Crack Properties

3.1. Methodology. Based on the experimental data, parameters such as crack density and aspect ratio are obtained with the DZ model [15]. These parameters can be used to characterize the pore distribution. The specific steps are given in Appendix A, and the flow chart is shown in Figure 5.

3.2. Crack Properties. The crack properties can be obtained by following the methodology presented in Section 3.1.

Figure 6 shows the crack density as a function of the effective pressure for twelve tight sandstones. The crack density gradually decreases with increasing pressure. When the pressure is low, the variation in crack density is significant.

The crack aspect ratio is not a constant, but a continuous distribution within a certain range [18]. However, the main

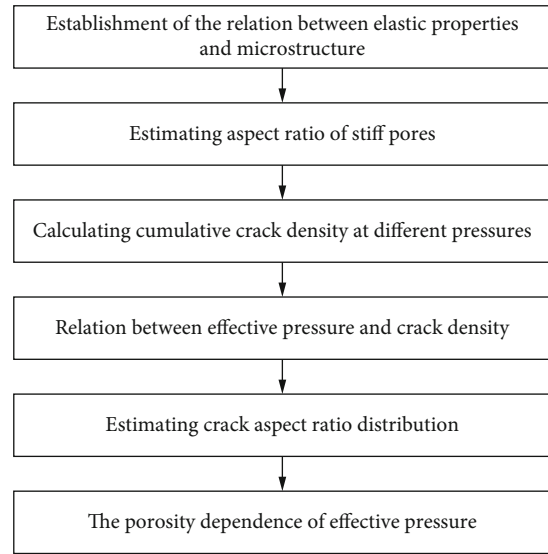


FIGURE 5: Rock parameter estimation flow chart.

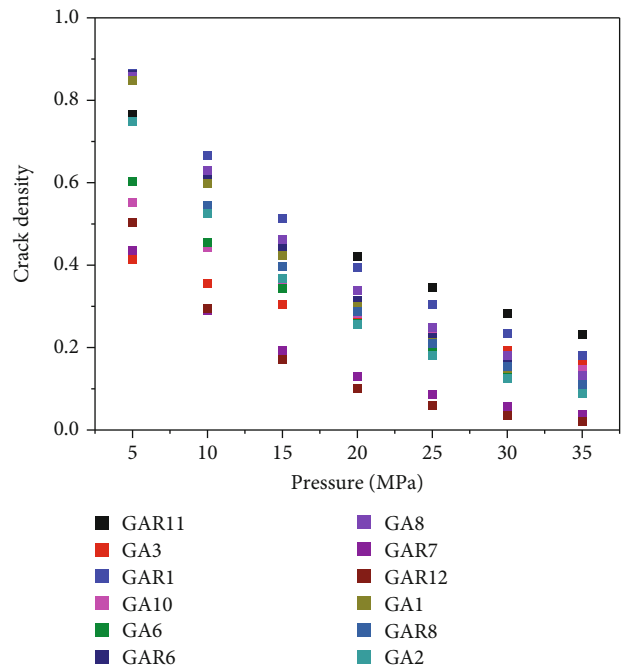


FIGURE 6: Crack density as a function of effective pressure in twelve tight sandstones.

crack aspect ratio is constant at a certain pressure, which is the aspect ratio corresponding to the peak of the curve [60]. The main crack aspect ratio of sample GAR7 for different pressures is shown in Figure 7, where we observe that the crack porosity decreases with increasing pressure, more pronounced at low pressures [18, 42, 61, 62]. The main reason is the closure of cracks.

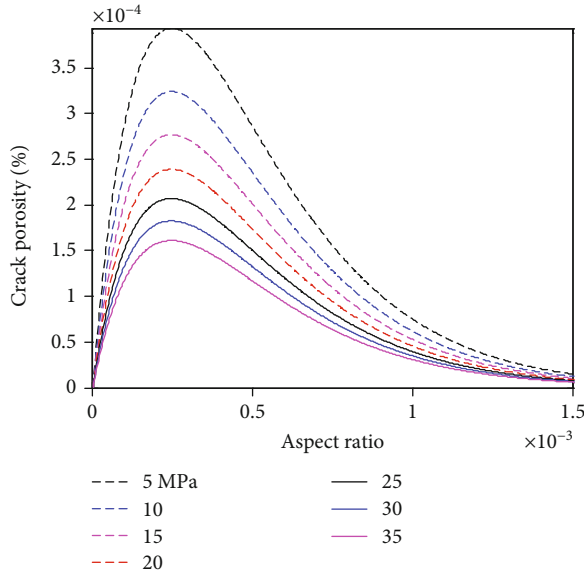


FIGURE 7: Crack porosity obtained with the DZ model based on experimental data as a function of main crack aspect ratio in GAR7 at different pressures.

4. The Squirt-Flow Length

4.1. MFS Model. The pore space can be classified into compliant pores (cracks and grain contacts) and stiff pores (intergranular voids), where the latter correspond to the main porosity [34, 59, 63]. A modified frame squirt-flow model is proposed according to the characteristics of the microscopic pore structure. The cracks are incorporated into an effective rock skeleton as shown in Figure 8, containing only stiff pores.

The MFS model is based on the theory of Dvorkin et al. [40], by applying the boundary condition of Gurevich et al. [35] (the boundary pressure at the contact between cracks and stiff pores is constant). The P-wave velocity predicted by this model is consistent with that from the Gassmann equation at low frequencies and approaches the high limit value (the rock without compliant pores) at high frequencies [41].

The modified-frame bulk modulus is

$$K_{ms} = K_{msd} + \frac{\alpha_c^2 F_c}{\phi_c} \left[1 - \frac{2J_1(\lambda R)}{\lambda R J_0(\lambda R)} \right], \quad (1)$$

where $K_{msd} = (1/K_0 - 1/K_{hp} + 1/K_{dry})^{-1}$, K_{dry} is the dry-rock bulk modulus, $F_c = (1/K_{fl} + 1/(\phi_c Q_c))^{-1}$, ϕ_c is crack porosity, $\alpha_c = 1 - K_{msd}/K_0$, $Q_c = K_0/(\alpha_{md} - \phi_c)$, $\alpha_{md} = 1 - K_{md}/K_0$ is the poroelasticity coefficient, J_0 and J_1 are the zero- and first-order Bessel functions, respectively, $\lambda^2 = i\omega\eta\phi_c/\kappa(1/K_{fl} + 1/(\phi_c Q_c))$, ω is angular frequency, η is the fluid viscosity, κ is permeability, and K_{fl} is the fluid bulk modulus.

Then, the modified dry-rock bulk and shear moduli are

$$\begin{aligned} \frac{1}{K_{md}} &= \frac{1}{K_{ms}} + \frac{1}{K_{hp}} - \frac{1}{K_0}, \\ \frac{1}{\mu_{md}} &= \frac{1}{\mu_{dry}} - \frac{4}{15} \left(\frac{1}{K_{dry}} - \frac{1}{K_{md}} \right), \end{aligned} \quad (2)$$

respectively, where K_{hp} is the bulk modulus of the dry rock when all the cracks are closed, which can be obtained by fitting the dry-rock velocity with effective pressure [35], and μ_{dry} is the dry-rock shear modulus. The P-wave velocity and attenuation of the fluid-saturated rock can be obtained according to Toksöz and Johnston [64]:

$$V_{phP1,2} = \frac{1}{\text{Re}(X_{1,2})}, \quad a_{1,2} = \omega \text{Im}(X_{1,2}), \quad (3)$$

where

$$\begin{aligned} X_{1,2} &= \sqrt{Y_{1,2}}, \quad Y_{1,2} = -\frac{B}{2A} \pm \sqrt{\left(\frac{B}{2A}\right)^2 - \frac{C}{A}}, \quad A = \frac{\phi F M_{dry}}{\rho_s^2}, \\ B &= \frac{F(2\alpha_{md} - \phi - \phi(\rho_1/\rho_2)) - (M_{dry} + F(\alpha_{md}^2/\phi))(1 + \rho_a/\rho_2 + i(\omega_c/\omega))}{\rho_2}, \\ C &= \frac{\rho_1}{\rho_2} + \left(1 + \frac{\rho_1}{\rho_2}\right) \left(\frac{\rho_a}{\rho_2} + i\frac{\omega_c}{\omega}\right), \quad \rho_1 = (1 - \phi)\rho_s, \quad \rho_2 = \phi\rho_{fl}, \\ F &= \left(\frac{1}{K_{fl}} + \frac{(\alpha_{md} - \phi)}{(\phi K_0)}\right)^{-1}, \end{aligned} \quad (4)$$

where ρ_a is the additional coupling density, $\omega_c = \eta\phi/(\kappa\rho_{fl})$ is the characteristic frequency, $\alpha_{md} = 1 - K_{md}/K_0$, ϕ the is porosity, M_{dry} is the uniaxial modulus of the rock skeleton at drained conditions, ρ_s is the mineral density, and ρ_{fl} is fluid density.

Figure 9 shows the P-wave velocity of sample GAR7 as a function of frequency and different pressures, where R is computed with the least-square method (see Table 2 in Appendix B), by minimizing square of difference between the experimental data and P-wave velocity predicted by the MFS model. From 5 to 35 MPa, R takes the following values: 0.055, 0.051, 0.049, 0.044, 0.041, 0.038, and 0.03 (in mm). The fluid properties of the fluid are those at the measurement conditions according to Batzle and Wang [65]. The bulk and shear moduli of the dry rock are obtained from the velocity and density. The P-wave velocity dispersion decreases with increasing pressure.

4.2. Squirt-Flow Length. Figure 10 shows the P-wave velocity as a function of the effective pressure, where R is obtained as described above (see Table 3 in Appendix B).

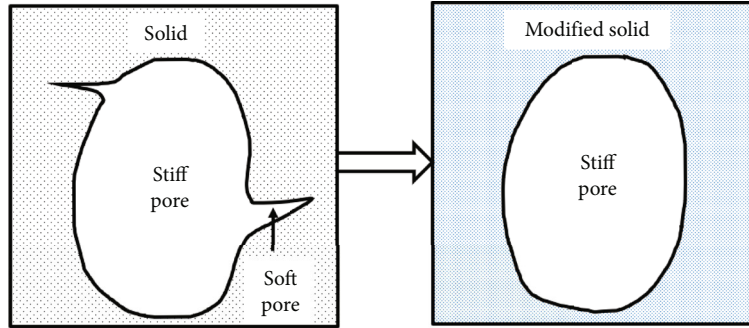


FIGURE 8: Modified rock skeleton.

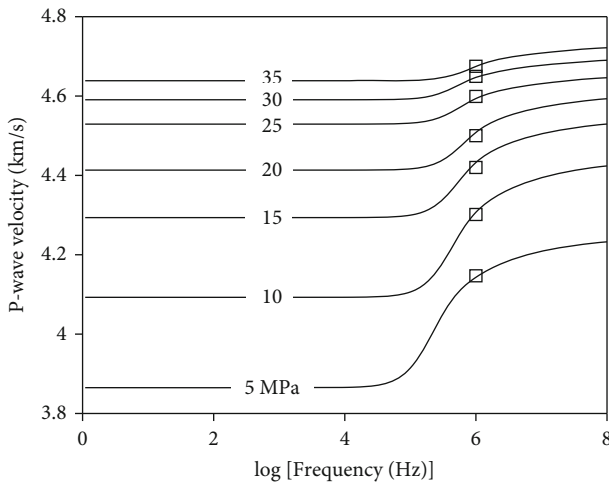


FIGURE 9: P-wave velocity predicted by the MFS model as a function of frequency at different effective pressures, where the squares correspond to experimental data at full water saturation.

It is seen that the P-wave velocity predicted by the model increases with the squirt-flow length. For most of the samples (GAR11, GAR6, GA8, GAR7, GAR12, GA1, GAR8, and GA2), R decreases as pressure increases. The main reason is that the cracks with smaller aspect ratios tend to close. In samples GA3, GAR1, GA10, and GA6, R increases with increasing pressure. The pressure is not the only factor affecting the squirt-flow length. These tight samples show different characteristics of fabric heterogeneity. The mineral composition, pore/microcrack shape/scale, grain scale, and their distributions all effect on the acoustic wave velocities. We adopt a single R in the model predictions for each sample, which in fact assumes a unique microcrack scale for the proposed idealized rock model. However, for those samples with a higher degree of fabric heterogeneity (i.e., containing more types of different microcracks, specifically with different scales), the model prediction may deviate more from the experimental measurement than those with a lower heterogeneity degree. Figure 10 shows the velocity as a function of frequency for the different samples at different pressures and the optimal squirt-flow length. It shows that each sample is approximately characterized by a constant R at different pressures. Thus, R can be considered as an intrinsic

property of the rock [32]. The appropriate squirt-flow lengths of the twelve samples are 0.015, 0.035, 0.02, 0.023, 0.15, 0.12, 0.22, 0.045, 0.25, 0.35, 0.25, and 0.28 (in mm) and mainly occur between 10 and 25 MPa. In order to improve the estimation, R can be calculated by using the P- and S-wave velocities in this pressure range.

The comparison between the MFS model results and experimental data is shown in Figure 11, based on R reported in Figure 10. In samples GAR11, GAR6, GA8, GAR7, GAR12, GA1, GAR8, and GA2, at low frequencies, the predicted P-wave velocity is lower than the experimental data. With increasing pressure, the prediction gradually approaches the experimental data. For samples GA3, GAR1, GA10, and GA6, the result is higher than the experimental data in the low-pressure range. As pressure increases, the result approaches the experimental data.

4.3. Squirt-Flow Length and Crack Properties. Based on the experimental data, the factors influencing the squirt flow are analyzed with the MFS model. Figures 12–14 show R as a function of crack density, main crack aspect ratio, and permeability, respectively, for the twelve rock samples. The results show that R increases with increasing crack density and permeability and decreases with increasing crack aspect ratio. Cheng et al. [66] showed that the crack fraction and its radius increase with total porosity. Consequently, a higher crack fraction and flow length enhance the effect of the local fluid flow induced by the waves.

Crack density and aspect ratio are the main parameters to represent the effect of cracks, since they affect R [67]. Basically, the analysis shows that there is an optimal value of R within a certain pressure range for a given sample. Permeability also affects R (see Figure 15).

The characteristic frequency of the squirt flow and the critical diffusion length can be used to determine the squirt-flow length. The first is given by [35, 68, 69], and [37].

$$f_c = \gamma^3 \frac{K_0}{\eta} \quad (5)$$

Mavko and Mukerji [70] report a critical diffusion length.

$$l_c = \sqrt{\frac{\kappa K_0}{\eta f_c}} \quad (6)$$

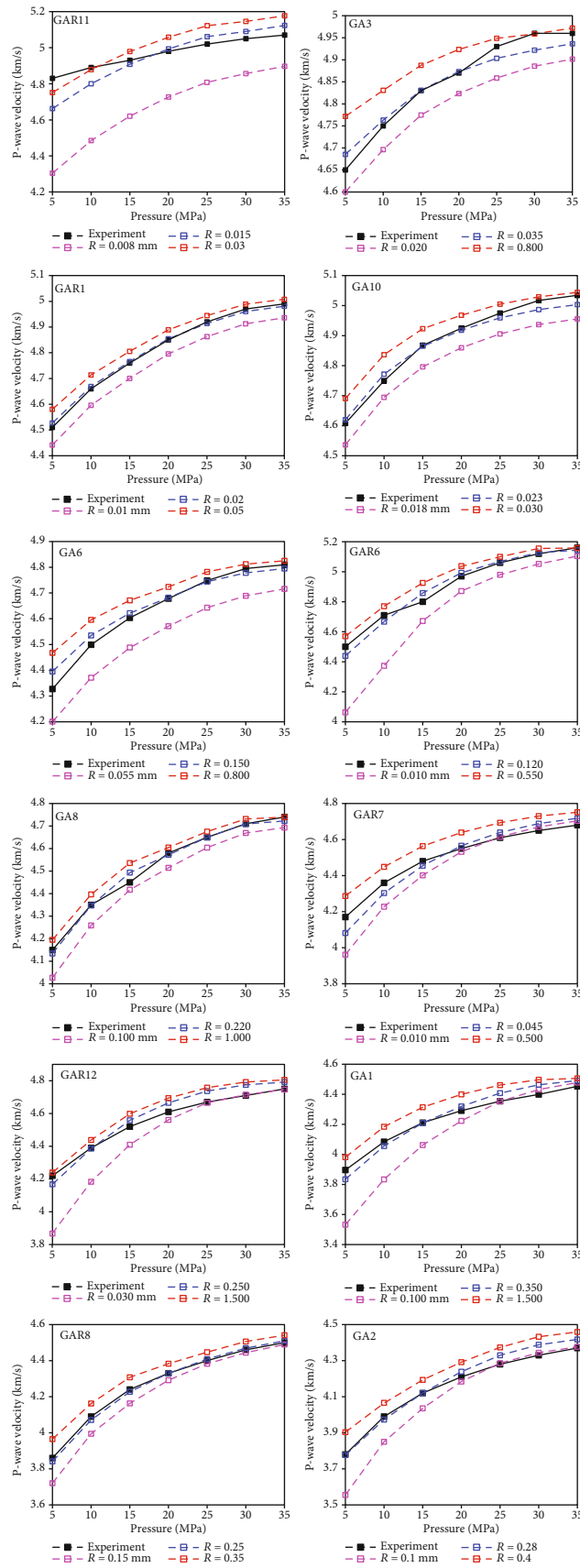


FIGURE 10: P-wave velocities predicted by the MFS model as a function of the effective pressure compared with the experimental data of full water saturation giving different squirt-flow lengths.

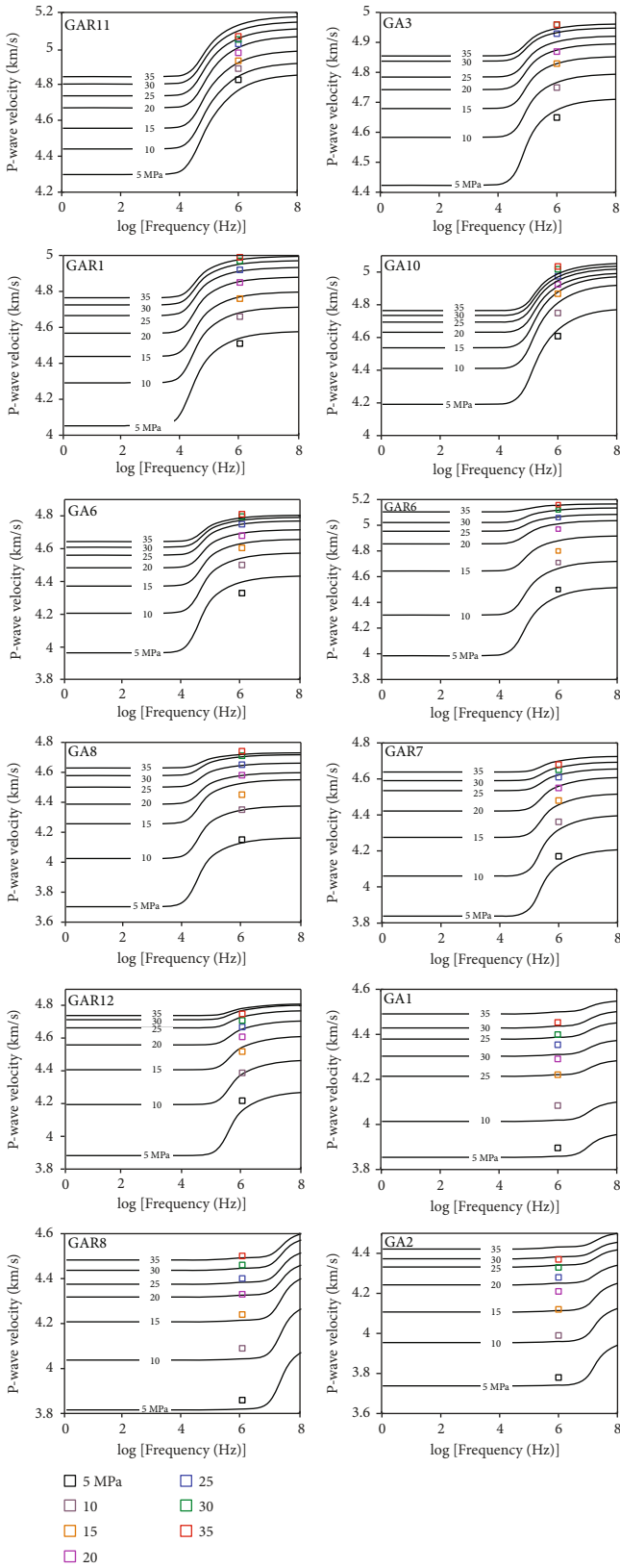


FIGURE 11: P-wave velocities predicted by the MFS model as a function of frequency compared with the experimental data (squares) for different pressures at full water saturation.

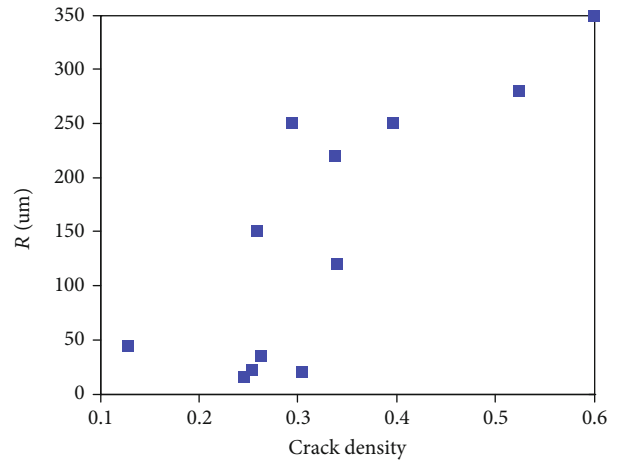


FIGURE 12: R as a function of crack density.

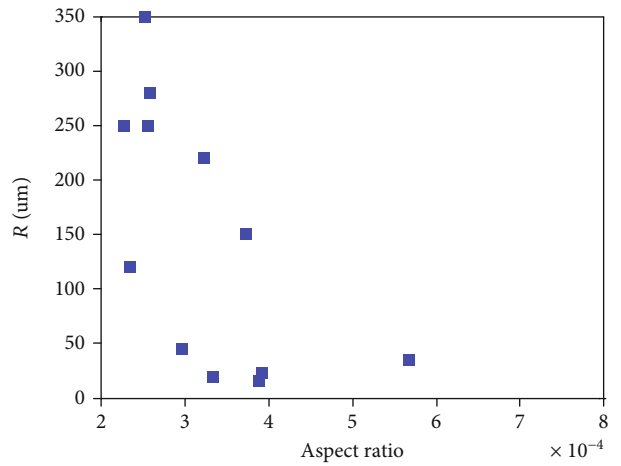


FIGURE 13: R as a function of the main crack aspect ratio.

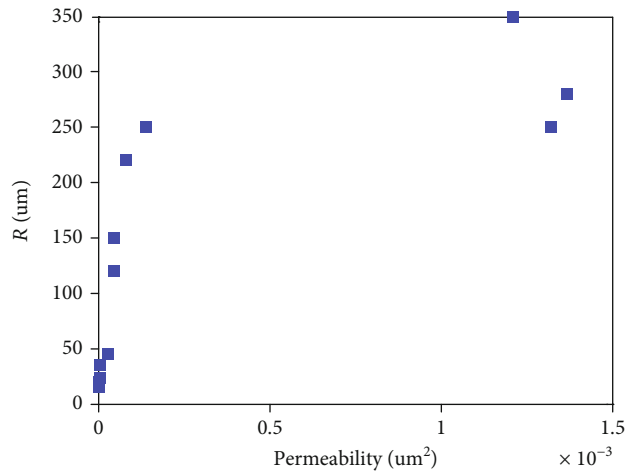


FIGURE 14: R as a function of permeability.

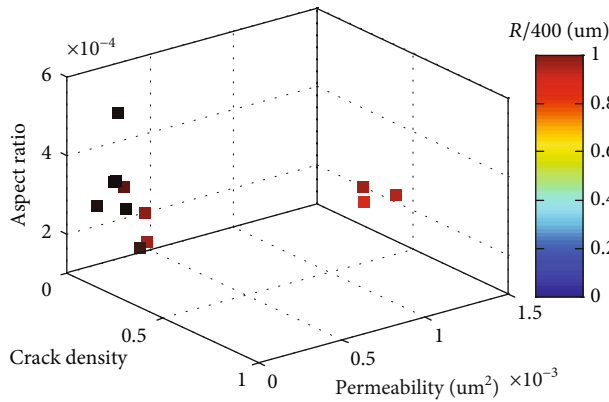


FIGURE 15: R as a function of crack density, crack aspect ratio, and permeability, corresponding to the twelve samples.

According to Equations (5) and (6), we have

$$l_c = \sqrt{\frac{\kappa K_{fl}}{K_0 \gamma^3}}. \quad (7)$$

When the diffusion length is less than the critical one, the pore-fluid pressure has sufficient time to reach an equilibrium (relaxed state); otherwise, the pore fluid pressure cannot reach equilibrium, and the regime is unrelaxed.

According to Pride [71] and Dvorkin and Nur [32] and the previous analysis, we find that R is proportional to permeability and crack density and inversely proportional to the main crack aspect ratio.

In this work, we assume a semiempirical equation.

$$R = a \sqrt{\frac{\kappa K_{fl}}{K_0 \gamma^3}} \Gamma + b. \quad (8)$$

The parameters a and b can be obtained by fitting experimental data and can be different for different lithologies and facies. Based on the twelve tight sandstones, we obtain

$$R = 0.03856 \sqrt{\frac{\kappa K_{fl}}{K_0 \gamma^3}} \Gamma + 63.42. \quad (9)$$

Equation (9) is represented in Figure 16, where we can see that R increases with the increase of crack density and permeability, when the crack density and permeability increase, and decreases with the increase of main crack aspect ratio, and the characteristic frequency of squirt flow moves to low frequencies (relaxed state) [32, 35, 40, 67, 71].

R is considered an intrinsic property, and Equation (9) provides a quantitative way for its determination. The property cannot be measured directly. However, it can be obtained by experiment using a suitable rock-physics model.

5. Conclusions

The sandstones in Guang'an area have low porosity and permeability and strong heterogeneities with microcracks and

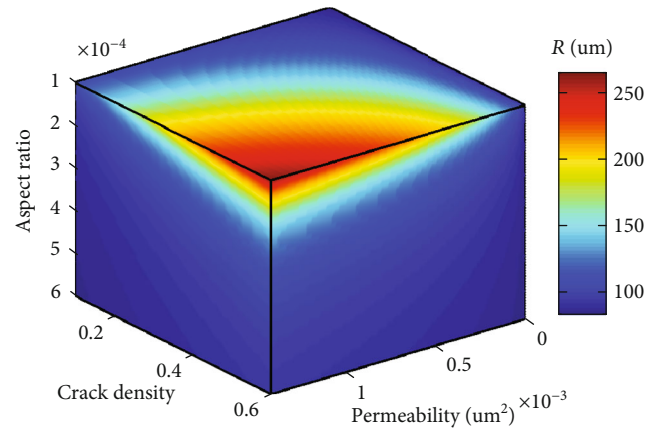


FIGURE 16: R as a function of crack density, crack aspect ratio, and permeability. The correlation coefficient is 0.877, and the average difference between R predicted with the experimental data and the semiempirical equation is 16.4%.

can be considered as a typical type of tight sandstone. We have proposed a rock-physics model to estimate the squirt-flow length (R) of tight sandstones, based on experiment data. The crack density and aspect ratio and frame permeability are obtained with effective-medium theories. We establish a semiempirical equation relating these quantities to the squirt-flow length, based on ultrasonic experimental data. The results show that R increases with increasing crack density and permeability and decreases with increasing crack aspect ratio. The methodology provides a new method for the calculation of R in tight sandstones, which can also be applied to other lithologies, e.g., carbonates. In a seismic exploration context, even an approximate estimation of R from seismic velocities measured at a single frequency is useful, as this allows one to infer derived parameters such as crack density, aspect ratio, and permeability, by using rock physics models.

Appendix

Figure 9 shows the P-wave velocity of sample GAR7 as a function of frequency and different pressures, where R is computed with the least-square method (see Table 2 in Appendix B, which gives the minimum square of difference between P-wave velocity prediction of the MFS model and experimental data of sample (GAR7) under different effective pressures), by minimizing square of difference between the experimental data and P-wave velocity predicted by the MFS model.

Figure 10 shows the P-wave velocity as a function of the effective pressure, where R is obtained as described above (see Table 3 in Appendix B, which gives the minimum square of difference between experimental data and P-wave velocity predicted by the MFS model and the relative difference between experimental data and model prediction for each rock in Figure 10).

A. Estimation of the Rock Properties

Step 1. Calculate the aspect ratio of the stiff pores. Based on the MT model, the quantitative relationship between elastic

moduli and stiff porosity is established. The effective moduli are

$$\frac{1}{K_{\text{stiff}}^{\text{MT}}} = \frac{1}{K_0} \left(1 + \frac{\phi_s}{1 - \phi_s} P \right), \quad (\text{A.1})$$

$$\frac{1}{\mu_{\text{stiff}}^{\text{MT}}} = \frac{1}{\mu_0} \left(1 + \frac{\phi_s}{1 - \phi_s} Q \right), \quad (\text{A.2})$$

where $K_{\text{stiff}}^{\text{MT}}$ and $\mu_{\text{stiff}}^{\text{MT}}$ are the bulk and shear moduli of the rock only containing stiff pores, K_0 and μ_0 are the bulk and shear moduli of the mineral mixture, respectively, ϕ_s is the stiff porosity, and

$$P = \frac{(1 - \nu)}{6(1 - 2\nu)} \times \frac{4(1 + \nu) + 2\gamma^2(7 - 2\nu) - [3(1 + 4\nu) + 12\gamma^2(2 - \nu)]g}{2\gamma^2 + (1 - 4\gamma^2)g + (\gamma^2 - 1)(1 + \gamma)g^2},$$

$$Q = \frac{4(\gamma^2 - 1)(1 - \nu)}{15\{8(\gamma - 1) + 2\gamma^2(3 - 4\nu) + [(7 - 8\nu) - 4\gamma^2(1 - 2\nu)]g\}} \times \left\{ \frac{8(1 - \nu) + 2\gamma^2(3 + 4\nu) + [(8\nu - 1) - 4\gamma^2(5 + 2\nu)]g + 6(\gamma^2 - 1)(1 + \nu)g^2}{2\gamma^2 + (1 - 4\gamma^2)g + (\gamma^2 - 1)(1 + \gamma)g^2} - 3 \left[\frac{8(\nu - 1) + 2\gamma^2(5 - 4\nu) + [3(1 - 2\nu) + 6\gamma^2(\nu - 1)]g}{-2\gamma^2 + [(2 - \gamma) + \gamma^2(1 + \nu)]g} \right] \right\},$$

$$g = \begin{cases} \frac{\gamma}{(1 - \gamma^2)^{3/2}} (\arccos \gamma - \gamma\sqrt{1 - \gamma^2}) (\gamma < 1), \\ \frac{\gamma}{(1 - \gamma^2)^{3/2}} (\gamma\sqrt{1 - \gamma^2} - \operatorname{arccosh} \gamma) (\gamma > 1), \end{cases} \quad (\text{A.3})$$

where γ is the spheroidal aspect ratio and ν is the Poisson ratio of the grains, i.e., $\nu = (3K_0 - 2\mu_0)/(6K_0 + 2\mu_0)$.

Cracks are introduced into the host material, by neglecting the interactions between cracks and pores. The effective moduli are

$$\frac{1}{K_{\text{eff}}^{\text{MT}}} = \frac{1}{K_{\text{stiff}}^{\text{MT}}} \left(1 + \frac{16(1 - (\nu_{\text{stiff}}^{\text{MT}})^2)\Gamma}{9(1 - 2\nu_{\text{stiff}}^{\text{MT}})} \right), \quad (\text{A.4})$$

$$\frac{1}{\mu_{\text{eff}}^{\text{MT}}} = \frac{1}{\mu_{\text{stiff}}^{\text{MT}}} \left(1 + \frac{32(1 - \nu_{\text{stiff}}^{\text{MT}})(5 - \nu_{\text{stiff}}^{\text{MT}})\Gamma}{45(2 - \nu_{\text{stiff}}^{\text{MT}})} \right), \quad (\text{A.5})$$

where $\nu_{\text{stiff}}^{\text{MT}}$ is the Poisson ratio of the rock with only stiff pores, i.e., $\nu_{\text{stiff}}^{\text{MT}} = (3K_{\text{stiff}}^{\text{MT}} - 2\mu_{\text{stiff}}^{\text{MT}})/(6K_{\text{stiff}}^{\text{MT}} + 2\mu_{\text{stiff}}^{\text{MT}})$, $K_{\text{eff}}^{\text{MT}}$ and $\mu_{\text{eff}}^{\text{MT}}$ are the effective bulk and shear moduli, respectively, when the rock contains cracks and stiff pores, and Γ is the crack density. All the cracks close at high effective pressure, so that there are only stiff pores. The least-square method is used to obtain the optimal aspect ratio of the stiff pores by using Equations (A.1) and (A.2) (see Table 4 in Appendix B).

Step 2. Calculate the cumulative crack density at different pressures. It can be obtained with Equations (A.4) and (A.5) by a least-square method (see Table 5 in Appendix B). When this is known, the moduli can be obtained.

Step 3. Establish the relation between effective pressure and crack density, which can be determined by using the relation between the crack density and effective pressure [58]:

$$\Gamma = \Gamma^i e^{-P/P^{\wedge}}, \quad (\text{A.6})$$

where Γ^i is the initial value when the effective pressure is zero and P^{\wedge} is a constant.

Step 4. Calculate the crack aspect ratio distribution. When the effective pressure increases, cracks gradually tend to close. The minimum initial aspect ratio of the unclosed cracks under each effective pressure can be obtained as [14]

$$\gamma^i = \frac{3}{4\pi} \int_{\Gamma^i}^{\Gamma} \frac{(1/K(\Gamma) - 1/K_{\text{eff}}^{\text{hp}}) dp}{\Gamma} d\Gamma, \quad (\text{A.7})$$

where $K(\Gamma)$ is the effective bulk modulus at different pressures, which can be computed from Equation (A.1).

Substituting Equation (A.8) into (A.9), we obtain

$$\gamma^i = \frac{3}{4\pi} \int_{\Gamma(\gamma)}^{\Gamma^i} \frac{(1/K(\Gamma) - 1/K_{\text{eff}}^{\text{hp}}) \hat{p}}{\Gamma^2} d\Gamma, \quad (\text{A.8})$$

and integrating Equation (A.10) from Γ to Γ^i ,

$$\gamma^i = \frac{4\hat{p} \left[1 - \left(\nu_{\text{eff}}^{\text{hp}} \right)^2 \ln(\Gamma^i/\Gamma) \right]}{3\pi K_{\text{eff}}^{\text{hp}} \left[1 - 2\nu_{\text{eff}}^{\text{hp}} \right]}, \quad (\text{A.9})$$

where $\nu_{\text{eff}}^{\text{hp}}$ is the effective Poisson ratio at high pressures, i.e., $\nu_{\text{eff}}^{\text{hp}} = (3K_{\text{eff}}^{\text{hp}} - 2\mu_{\text{eff}}^{\text{hp}})/(6K_{\text{eff}}^{\text{hp}} + 2\mu_{\text{eff}}^{\text{hp}})$.

Combined with Equations (A.6) and (A.9), the relation between the minimum initial aspect ratio and the effective pressure can be obtained:

$$\gamma^i = \frac{4 \left[1 - \left(\nu_{\text{eff}}^{\text{hp}} \right)^2 \right] p}{\pi E_{\text{eff}}^{\text{hp}}}, \quad (\text{A.10})$$

where $E_{\text{eff}}^{\text{hp}}$ is the effective Young modulus at high pressures, i.e., $E_{\text{eff}}^{\text{hp}} = 3K_{\text{eff}}^{\text{hp}}[1 - 2\nu_{\text{eff}}^{\text{hp}}]$. The cumulative crack density decreases when the effective pressure increases. If the effective pressure changes from zero to dp , the corresponding reduction of cumulative crack density is $d\Gamma$. When the effective-pressure increment is small enough, the reduction of crack density can be considered to be caused by the closure of the cracks with aspect ratio less than the minimum initial aspect ratio. David and Zimmerman [14] relate crack porosity and crack density as

$$\phi_c = \frac{4\pi\gamma}{3} \Gamma. \quad (\text{A.11})$$

Therefore, the crack properties in rock can be obtained from the wave velocities as a function of the pressure from experimental measurements (e.g., [25]).

B. The Results of Least Square Method and Misfit for Each Rock over the Whole Pressure Range

TABLE 2: The minimum square of difference between P-wave velocity prediction of the MFS model and experimental data ($S_{\epsilon_4^2}$) of sample (GAR7) under different effective pressures.

Pressure	$S_{\epsilon_4^2}$	Pressure	$S_{\epsilon_4^2}$
5 MPa	1.48×10^{-5}	25 MPa	2.83×10^{-5}
10 MPa	3.18×10^{-5}	30 MPa	1.94×10^{-7}
15 MPa	1.56×10^{-4}	35 MPa	1.95×10^{-7}
20 MPa	6.49×10^{-5}		

TABLE 3: The minimum square of difference between experimental data and P-wave velocity predicted by the MFS model ($S_{\epsilon_3^2}$) and the relative difference between experimental data and model prediction for each rock over the whole pressure range in Figure 10 (E_r).

Sample	$S_{\epsilon_3^2}$	E_r	Sample	$S_{\epsilon_3^2}$	E_r
GAR11	0.0430	0.0869	GA8	0.0025	0.0198
GA3	0.0042	0.029	GAR7	0.0158	0.0662
GAR1	0.0006	0.0127	GAR12	0.0177	0.0706
GA10	0.0028	0.0244	GA1	0.0138	0.0652
GA6	0.0068	0.0359	GAR8	0.0011	0.0189
GAR6	0.0098	0.0455	GA2	0.0092	0.0479

TABLE 4: Aspect ratio of the stiff pores (γ_{stiff}) and the minimum square of difference between wave velocity prediction and experimental data ($S_{\epsilon_1^2}$).

Sample	γ_{stiff}	$S_{\epsilon_1^2}$	Sample	γ_{stiff}	$S_{\epsilon_1^2}$
GAR11	0.15	0.015	GA8	0.14	0.007
GA3	0.05	0.0357	GAR7	0.08	0.0111
GAR1	0.1	0.011	GAR12	0.06	0.006
GA10	0.14	0.0054	GA1	0.11	0.0137
GA6	0.07	0.0029	GAR8	0.31	0.0014
GAR6	0.26	0.0056	GA2	0.18	0.0033

TABLE 5: The minimum square of difference between wave velocity prediction and experimental data at different effective pressures ($S_{\epsilon_2^2}$).

Sample	$S_{\epsilon_2^2}$ (5 MPa)	$S_{\epsilon_2^2}$ (10 MPa)	$S_{\epsilon_2^2}$ (15 MPa)	$S_{\epsilon_2^2}$ (20 MPa)	$S_{\epsilon_2^2}$ (25 MPa)	$S_{\epsilon_2^2}$ (30 MPa)	$S_{\epsilon_2^2}$ (35 MPa)
GAR11	0.005	0.0085	0.0103	0.0107	0.0097	0.013	0.0123
GA3	0.003	0.007	0.0079	0.009	0.0087	0.011	0.0108
GAR1	0.0002	0.0003	0.0007	0.0047	0.0013	0.001	0.0011
GA10	0.0005	0.0003	0.0001	0.001	0.0017	0.0022	0.0024
GA6	0.00001	0.0002	0.0011	0.0015	0.0004	0.0007	0.0007
GAR6	0.0167	0.019	0.0287	0.0297	0.0287	0.0235	0.0314
GA8	0.0041	0.0032	0.0012	0.0018	0.0011	0.0002	0.0008
GAR7	0.0318	0.0283	0.0213	0.0183	0.0149	0.0125	0.0112
GAR12	0.0323	0.0271	0.0162	0.0119	0.0095	0.0077	0.0079
GA1	0.0007	0.0001	0.00008	0.00004	0.00008	0.0001	0.0005
GAR8	0.0011	0.0007	0.0005	0.00003	0.0001	0.0002	0.0005
GA2	0.000004	0.00003	0.0005	0.0006	0.0017	0.0029	0.0021

Data Availability

The data of the modeling results can be accessed by contacting the corresponding author.

Conflicts of Interest

The authors declare that they have no conflicts of interest.

Acknowledgments

This work is supported by the National Natural Science Foundation of China (grant nos. 41974123 and 42174161), the Jiangsu Province Science Fund for Distinguished Young Scholars (grant no. BK20200021), and the Sinopec Key Laboratory of Geophysics.

References

- [1] C. Z. Jia, "Breakthrough and significance of unconventional oil and gas to classical petroleum geology theory," *Petroleum Exploration and Development*, vol. 44, no. 1, pp. 1–10, 2017.
- [2] A. L. Khlaifat, H. Qutob, and N. Barakat, "Tight Gas Sands Development Is Critical to Future World Energy Resources," in *81st Ann. Society of Petroleum Engineers, Expanded Abstracts*, pp. 1–12, Muscat, Oman, 2011.
- [3] J. L. Wang, L. Y. Feng, M. Steve, X. Tang, T. E. Gail, and H. Mikael, "China's unconventional oil: A review of its resources and outlook for long-term production," *Energy*, vol. 82, pp. 31–42, 2015.
- [4] M. Q. Guo, J. Ba, R. P. Ma et al., "P-wave velocity dispersion and attenuation in fluid-saturated tight sandstones: characteristics analysis based on a double double-porosity structure model description," *Chinese Journal of Geophysics*, vol. 61, no. 3, pp. 1053–1068, 2018.
- [5] S. E. Laubach, P. Eichhubl, C. Hilgers, and R. H. Lander, "Structural diagenesis," *Journal of Structural Geology*, vol. 32, no. 12, pp. 1866–1872, 2010.
- [6] J. E. Olson, S. E. Laubach, and R. H. Lander, "Natural fracture characterization in tight gas sandstones: integrating mechanics and diagenesis," *AAPG Bulletin*, vol. 93, no. 11, pp. 1535–1549, 2009.
- [7] M. Q. Pang, J. Ba, J. M. Carcione, A. Vesnaver, R. P. Ma, and T. S. Chen, "Analysis of attenuation rock-physics template of tight sandstones," *Reservoir Microcrack Prediction*, vol. 63, no. 11, pp. 4205–4219, 2020.
- [8] Z. K. Xiao, W. L. Ding, J. S. Liu et al., "A fracture identification method for low-permeability sandstone based on R/S analysis and the finite difference method: A case study from the Chang 6 reservoir in Huaqing oilfield, Ordos Basin," *Journal of Petroleum Science and Engineering*, vol. 174, pp. 1169–1178, 2019.
- [9] B. Bai, R. Zhu, S. Wu et al., "Multi-scale method of Nano(Micro)-CT study on microscopic pore structure of tight sandstone of Yanchang Formation, Ordos Basin," *Ordos Basin, Petroleum Exploration and Development*, vol. 40, no. 3, pp. 354–358, 2013.
- [10] J. M. Carcione, *Wave Fields in Real Media: Theory and Numerical Simulation of Wave Propagation in Anisotropic, Anelastic, Porous and Electromagnetic Media*, Elsevier, 3rd edition, 2014.
- [11] T. M. Müller, B. Gurevich, and M. Lebedev, "Seismic wave attenuation and dispersion resulting from wave-induced flow in porous rocks — A review," *Geophysics*, vol. 75, no. 5, pp. 75A147–75A164, 2010.
- [12] Y. J. Song, H. S. Hu, J. W. Rudnicki, and Y. Duan, "Dynamic transverse shear modulus for a heterogeneous fluid-filled porous solid containing cylindrical inclusions," *Geophysical Journal International*, vol. 206, no. 3, pp. 1677–1694, 2016.
- [13] H. J. Yin, J. G. Zhao, G. Y. Tang, L. Zhao, X. Ma, and S. Wang, "Pressure and fluid Effect on frequency-dependent elastic moduli in fully saturated tight sandstone," *Journal of Geophysical Research: Solid Earth*, vol. 122, no. 11, pp. 8925–8942, 2017.
- [14] R. W. Zimmerman, *Compressibility of Sandstones*, Elsevier, Amsterdam, 1991.
- [15] E. C. David and R. W. Zimmerman, "Pore structure model for elastic wave velocities in fluid-saturated sandstones," *Journal of Geophysical Research: Solid Earth*, vol. 117, no. B7, article B07210, 2012.
- [16] T. Mori and K. Tanaka, "Die mittlere spannung in der matrix und die mittlere elastische energie von materialien mit einschlossen," *Acta Metallurgica*, vol. 21, no. 5, pp. 571–574, 1973.
- [17] J. G. Berryman, "Single-scattering approximations for coefficients in Biot's equations of poroelasticity," *The Journal of the Acoustical Society of America*, vol. 91, no. 2, pp. 551–571, 1992.
- [18] J. X. Deng, H. Zhou, H. Wang et al., "The influence of pore structure in reservoir sandstone on dispersion properties of elastic waves," *Chinese Journal of Geophysics*, vol. 58, no. 9, pp. 3389–3400, 2015.
- [19] Y. J. Wei, J. Ba, R. P. Ma, L. Zhang, C. Jm, and M. Guo, "Effective of effective pressure change on pore structure and elastic wave responses," *Chinese Journal of Geophysics*, vol. 63, no. 7, pp. 2810–2822, 2020.
- [20] S. Mochizuki, "Attenuation in partially saturated rocks," *Journal of Geophysical Research*, vol. 87, no. B10, pp. 8598–8604, 1982.
- [21] M. S. Sams, J. P. Neep, M. H. Worthington, and M. S. King, "The measurement of velocity dispersion and frequency-dependent intrinsic attenuation in sedimentary rocks," *Geophysics*, vol. 62, no. 5, pp. 1456–1464, 1997.
- [22] K. W. Winkler, "Dispersion analysis of velocity and attenuation in Berea sandstone," *Journal of Geophysical Research*, vol. 90, no. B8, pp. 6793–6800, 1985.
- [23] K. W. Winkler, "Estimates of velocity dispersion between seismic and ultrasonic frequencies," *Geophysics*, vol. 51, no. 1, pp. 183–189, 1986.
- [24] J. Ba, J. M. Carcione, and J. Nie, "Biot-Rayleigh theory of wave propagation in double-porosity media," *Journal of Geophysical Research*, vol. 116, no. B6, article B06202, 2011.
- [25] J. Ba, W. Xu, L. Y. Fu, J. M. Carcione, and L. Zhang, "Rock anelasticity due to patchy saturation and fabric heterogeneity: A double double-porosity model of wave propagation," *Journal of Geophysical Research-solid Earth*, vol. 122, no. 3, pp. 122–150, 2017.
- [26] L. Zhang, J. Ba, L. Fu, J. M. Carcione, and C. Cao, "Estimation of pore microstructure by using the static and dynamic moduli," *International Journal of Rock Mechanics and Mining Sciences*, vol. 113, pp. 24–30, 2019.
- [27] L. Zhang, J. Ba, and J. M. Carcione, "A rock-physics model to determine the pore microstructure of cracked porous rocks,"

- Geophysical Journal International*, vol. 223, no. 1, pp. 622–631, 2020.
- [28] D. H. Yang and Z. J. Zhang, “Effects of the Biot and the squirt-flow coupling interaction on anisotropic elastic waves,” *Chinese Science Bulletin*, vol. 45, no. 23, pp. 2130–2138, 2000.
- [29] M. A. Biot, “Theory of propagation of elastic waves in a fluid-saturated porous Solid. I. Low-Frequency range,” *Journal of the Acoustical Society America*, vol. 28, no. 2, pp. 168–178, 1956.
- [30] M. A. Biot, “Theory of propagation of elastic waves in a fluid-saturated porous Solid. II. higher frequency range,” *Journal of the Acoustical Society America*, vol. 28, no. 2, pp. 179–191, 1956.
- [31] M. A. Biot, “Mechanics of deformation and acoustic propagation in porous media,” *Journal of Applied Physics*, vol. 33, no. 4, pp. 1482–1498, 1962.
- [32] J. Dvorkin and A. Nur, “Dynamic poroelasticity: a unified model with the squirt and the Biot mechanisms,” *Geophysics*, vol. 58, no. 4, pp. 524–533, 1993.
- [33] F. Gassmann, “Über die elasticität poröser medien,” *Vierteljahrsschrift: der Naturforschenden Gesellschaft Zürich*, vol. 96, pp. 1–23, 1951.
- [34] G. Mavko and D. Jizba, “Estimating grain-scale fluid effects on velocity dispersion in rocks,” *Geophysics*, vol. 56, no. 12, pp. 1940–1949, 1991.
- [35] B. Gurevich, D. Makarynska, O. B. de Paula, and M. Pervukhina, “A simple model for squirt-flow dispersion and attenuation in fluid-saturated granular rocks,” *Geophysics*, vol. 75, no. 6, pp. N109–N120, 2010.
- [36] W. F. Murphy, K. W. Winkler, and R. L. Kleinberg, “Acoustic relaxation in sedimentary rocks, dependence on grain contacts and fluid saturation,” *Geophysics*, vol. 51, no. 3, pp. 757–766, 1986.
- [37] D. Q. Li, J. X. Wei, B. di, P. Ding, S. Huang, and D. Shuai, “Experimental study and theoretical interpretation of saturation effect on ultrasonic velocity in tight sandstones under different pressure conditions,” *Geophysical Journal International*, vol. 212, no. 3, pp. 2226–2237, 2018.
- [38] J. M. Carcione and B. Gurevich, “Differential form and numerical implementation of Biot’s poroelasticity equations with squirt dissipation,” *Geophysics*, vol. 76, no. 6, pp. N55–N64, 2011.
- [39] C. Zener, *Elasticity and Anelasticity of Metals*, University of Chicago Press, Chicago, 1948.
- [40] J. Dvorkin, G. Mavko, and A. Nur, “Squirt flow in fully saturated rocks,” *Geophysics*, vol. 60, no. 1, pp. 97–107, 1995.
- [41] C. F. Wu, J. Ba, J. M. F. Carcione, L. Y. Fu, E. M. Chesnokov, and L. Zhang, “A squirt-flow theory to model wave anelasticity in rocks containing compliant microfractures,” *Physics of the Earth and Planetary Interiors*, vol. 301, article 106450, 2020.
- [42] F. Ouyang, J. G. Zhao, Z. Li et al., “Modeling velocity dispersion and attenuation using pore structure characteristics of rock,” *Chinese Journal of Geophysics*, vol. 64, no. 3, pp. 1034–1047, 2021.
- [43] J. Dvorkin, R. Nolen-Hoeksema, and A. Nur, “The squirt-flow mechanism: macroscopic description,” *Geophysics*, vol. 59, no. 3, pp. 428–438, 1994.
- [44] A. I. Best, *The Prediction of the Reservoir Properties of Sedimentary Rocks from Seismic Measurements*, [Ph.D. thesis], University of Reading, 1992.
- [45] G. Marketos and A. I. Best, “Application of the BISQ model to clay squirt flow in reservoir sandstones,” *Journal of Geophysical Research*, vol. 115, no. B6, article B06209, 2010.
- [46] M. S. Diallo and E. Appel, “Acoustic wave propagation in saturated porous media: reformulation of the Biot/squirt flow theory,” *Journal of Applied Geophysics*, vol. 44, no. 4, pp. 313–325, 2000.
- [47] M. S. Diallo, M. Prasad, and E. Appel, “Comparison between experimental results and theoretical predictions for P-wave velocity and attenuation at ultrasonic frequency,” *Wave Motion*, vol. 37, no. 1, pp. 1–16, 2003.
- [48] C. F. Wu, J. Ba, L. Zhang, and M. J. Carcione, “Anelasticity of porous rocks containing microcracks: a reformulation of the BISQ model,” *Bollettino di Geofisica Teorica ed Applicata*, vol. 60, no. 3, pp. 403–418, 2019.
- [49] D. H. Yang and Z. J. Zhang, “Poroelastic wave equation including the Biot/squirt mechanism and the solid/fluid coupling anisotropy,” *Wave Motion*, vol. 35, no. 3, pp. 223–245, 2002.
- [50] Y. Q. Sheng and D. H. Yang, “The green function of two-phase media BISQ model,” *Chinese Journal of Geophysics*, vol. 47, no. 1, pp. 101–105, 2004.
- [51] K. D. Yang, D. H. Yang, and S. Q. Wang, “Numerical simulation by staggered grid method for high frequency limited BISQ equation,” *Oil Geophysical Prospecting*, vol. 37, no. 5, pp. 463–468, 2002.
- [52] K. D. Yang, D. H. Yang, and S. Q. Wang, “Wave-Fields simulation based on the Biot-squirt equation,” *Chinese Journal of Geophysics*, vol. 45, no. 6, pp. 894–902, 2002.
- [53] A. N. Tutuncu, A. L. Podio, and M. M. Sharma, “An experimental investigation of factors influencing compressional and shear wave velocities and attenuations in tight gas sandstones,” *Geophysics*, vol. 59, no. 1, pp. 77–86, 1994.
- [54] M. Q. Guo, L. Y. Fu, and J. Ba, “Comparison of stress-associated coda attenuation and intrinsic attenuation from ultrasonic measurements,” *Geophysical Journal International*, vol. 178, no. 1, pp. 447–456, 2009.
- [55] X. F. Yan, F. C. Yao, H. Cao, J. Ba, L. L. Hu, and Z. F. Yang, “Analyzing the mid-low porosity sandstone dry frame in central Sichuan based on effective medium theory,” *Applied Geophysics*, vol. 8, no. 3, pp. 163–170, 2011.
- [56] A. Yurikov, M. Lebedev, and M. Pervukhina, “Ultrasonic velocity measurements on thin rock samples: experiment and numerical modeling,” *Geophysics*, vol. 83, no. 2, pp. MR47–MR56, 2018.
- [57] J. M. Carcione and G. Quiroga-Goode, “Some aspects of the physics and numerical modeling of Biot compressional waves,” *Journal of Computational Acoustics*, vol. 3, no. 4, pp. 261–280, 1995.
- [58] L. T. Song, Y. Wang, Z. H. Liu, and Q. Wang, “Elastic anisotropy characteristics of tight sands under different confining pressures and fluid saturation rates,” *Chinese Journal of Geophysics*, vol. 58, no. 9, pp. 3401–3411, 2015.
- [59] S. A. Shapiro, “Elastic piezosensitivity of porous and fractured rocks,” *Geophysics*, vol. 68, no. 2, pp. 482–486, 2003.
- [60] C. Sun, G. Tang, J. Fortin, J. Borgomano, and S. Wang, “Dispersion and attenuation of elastic wave velocities: impact of microstructure heterogeneity and local measurements,” *Journal of Geophysical Research: Solid Earth*, vol. 125, no. 12, 2020.
- [61] T. Long, J. G. Zhao, X. Z. Liu et al., “Cross-band rock physics measurement and theoretical modeling of carbonate rocks—study on the effective of different on the dispersion

- and attenuation of carbonate rocks,” *Chinese Journal of Geophysics*, vol. 63, no. 12, pp. 4502–4516, 2020.
- [62] Y. Sun and B. Gurevich, “Modeling the Effect of pressure on the moduli dispersion in fluid-saturated rocks,” *Journal of Geophysical Research: Solid Earth*, vol. 125, no. 8, 2020.
- [63] J. B. Walsh, “The effect of cracks on the compressibility of rock,” *Journal of Geophysical Research*, vol. 70, no. 2, pp. 381–389, 1965.
- [64] M. N. Toksöz and D. H. Johnston, *Seismic Wave Attenuation*, Society of Exploration Geophysicists, Geophysics reprint series, 1981.
- [65] M. Batzle and Z. Wang, “Seismic properties of pore fluids,” *Geophysics*, vol. 57, no. 11, pp. 1396–1408, 1992.
- [66] W. Cheng, J. Ba, L. Fu, and M. Lebedev, “Wave-velocity dispersion and rock microstructure,” *Journal of Petroleum Science and Engineering*, vol. 183, article 106466, 2019.
- [67] X. M. Tang, “A unified theory for elastic wave propagation through porous media containing cracks—an extension of Biot’s poroelastic wave theory,” *Science China Earth Sciences*, vol. 41, no. 6, pp. 784–795, 2011.
- [68] T. Jones, W. Murphy, and A. Nur, *Effectives of temperature and saturation on the velocity and attenuation of seismic waves in rocks: applications to geothermal reservoir evaluation*, Stanford University, Stanford, CA, USA, 1980.
- [69] R. J. O’Connell and B. Budiansky, “Measures of dissipation in viscoelastic media,” *Geophysical Research Letters*, vol. 5, no. 1, pp. 5–8, 1978.
- [70] G. Mavko and T. Mukerji, “Bounds on low-frequency seismic velocities in partially saturated rocks,” *Geophysics*, vol. 63, no. 3, pp. 918–924, 1998.
- [71] S. R. Pride, J. G. Berryman, and J. M. Harris, “Seismic attenuation due to wave-induced flow,” *Journal of Geophysical Research*, vol. 109, no. B1, article B01201, 2004.